ARTICLE

Structural Phase Transformation in Strained Monolayer MoWSe$_2$ Alloy

Amey Apte,[†,#] Vidya Kochat,[†,#] Pankaj Rajak,[‡,#] Aravind Krishnamoorthy,[‡] Praveena Manimunda,[§] Jordan A. Hachtel,[||] Juan Carlos Idrobo,[||] Syed Asif Syed Amanulla,[§] Priya Vashishta,[‡] Aiichiro Nakano,[‡] Rajiv K. Kalia,*[‡] Chandra Sekhar Tiwary,*[†,⊥] and Pulickel M. Ajayan*[†]

†Department of Materials Science and Nano Engineering, Rice University, Houston, Texas 77005, United States
‡Collaboratory for Advanced Computing and Simulations, Department of Physics and Astronomy, Department of Computer Science, Department of Chemical Engineering and Materials Science, and Department of Biological Sciences, University of Southern California, Los Angeles, California 90089-0242, United States
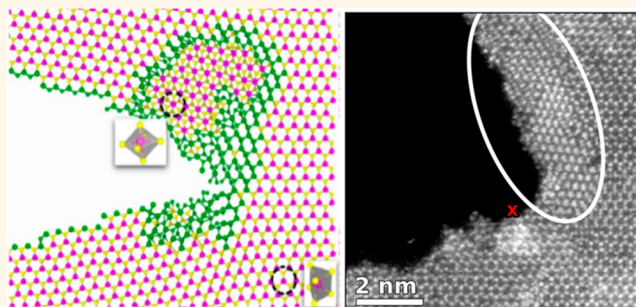§Bruker Nano Surfaces, Eden Prairie, Minnesota 55344, United States
||Center for Nanophase Materials Science, Oak Ridge National Laboratory, Oak Ridge, Tennessee 37831, United States
⊥Materials Science and Engineering, Indian Institute of Technology, Gandhinagar 382355, Gujarat, India

Ⓢ Supporting Information

ABSTRACT: Two-dimensional (2D) materials exhibit different mechanical properties from their bulk counterparts owing to their monolayer atomic thickness. Here, we have examined the mechanical behavior of 2D molybdenum tungsten diselenide (MoWSe$_2$) precipitation alloy grown using chemical vapor deposition and composed of numerous nanoscopic MoSe$_2$ and WSe$_2$ regions. Applying a bending strain blue-shifted the MoSe$_2$ and WSe$_2$ A$_{1g}$ Raman modes with the stress concentrated near the precipitate interfaces predominantly affecting the WSe$_2$ modes. *In situ* local Raman measurements suggested that the crack propagated primarily thorough MoSe$_2$-rich

regions in the monolayer alloy. Molecular dynamics (MD) simulations were performed to study crack propagation in an MoSe$_2$ monolayer containing nanoscopic WSe$_2$ regions akin to the experiment. Raman spectra calculated from MD trajectories of crack propagation confirmed the emergence of intermediate peaks in the strained monolayer alloy, mirroring experimental results. The simulations revealed that the stress buildup around the crack tip caused an irreversible structural transformation from the 2H to 1T phase both in the MoSe$_2$ matrix and WSe$_2$ patches. This was corroborated by high-angle annular dark-field images. Crack branching and subsequent healing of a crack branch were also observed in WSe$_2$, indicating the increased toughness and crack propagation resistance of the alloyed 2D MoWSe$_2$ over the unalloyed counterparts.

KEYWORDS: two-dimensional materials, transition-metal dichalcogenide, mechanical straining, Raman spectroscopy, molecular dynamics simulations

Two-dimensional (2D) materials represent an interesting subset of materials wherein a number of physical, chemical, electronic, and mechanical properties are drastically altered due to the spatial confinement of atoms and charge carriers to atomic thickness.[1−6] Since the graphene revolution, transition-metal dichalcogenides (TMDCs) have come of age, epitomizing the excellent properties of graphene in addition to certain advantages such as a direct optical band gap. TMDCs can exist in different hexagonal crystal polymorphs such as 2H, 1T, and 1T′. Like graphene, monolayer TMDCs are also expected to have interesting mechanical properties.

Experimentally obtained Young's moduli of suspended monolayer graphene and MoS$_2$ sheets *via* nanoindentation force−displacement experiments, for instance, have resulted in values of ~1120 GPa and ~270 GPa, respectively.[7−10] Apart from that, several efforts have been made in the recent past to mechanically deform these atomically thin sheets to tune optical bandgap as well.[11] However, the strain effects on monolayer TMDC alloys have not been explored well. The
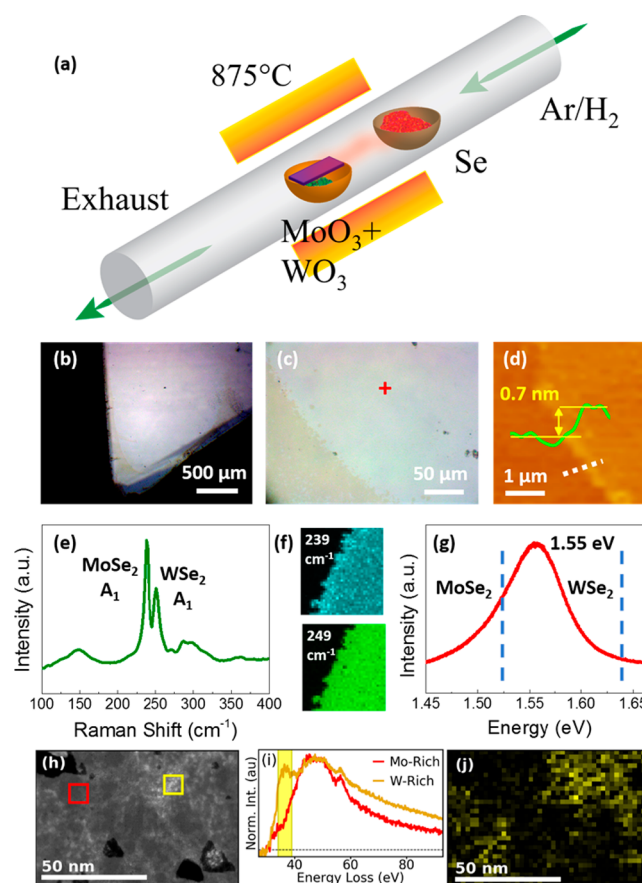
simultaneous presence of Mo and W chalcogenides in a 2D material can give rise to interesting behavior. To date the plastic deformation and fracture study of these atomically thin sheets have not been performed due to experimental challenges related to high sensitivity of TMDCs under electron beam and limited deformation in AFM. With an instrumented nano-indenter, one can apply larger force and displacements. Combining scanning probe microscopy (SPM) and Raman spectroscopy along with nanoindentation can be very useful in understanding bonding and deformation. Monolayer TMDCs have strong characteristic Raman modes arising from in-plane and out-of-plane oscillatory motion of atoms; these are the E^1_{2g} and A_{1g} phonon modes, respectively.[12] The role of Raman characterization during deformation becomes very important for alloy TMDCs without introducing any defects. The sulfide-based TMDCs display strong in-plane Raman-active modes which can be conveniently probed as a result; the corresponding selenides usually have very weak in-plane modes relative to the out-of-plane mode intensities. However, these characteristic modes have strong intensity and correlate well with the 2D nature of TMDCs. Moreover, applying strain on a 2D TMDC alloy can impart significant change in its structural symmetry, which can be probed via Raman spectroscopy and high-resolution scanning transmission electron microscopy (STEM).

In this work, we have grown a monolayer binary TMDC alloy of molybdenum tungsten diselenide ($MoWSe_2$) using chemical vapor deposition (CVD). The sample was grown on an atomically flat single crystal (0001) sapphire substrate that resulted in a large crystalline film spanning a couple of millimeters while maintaining monolayer thickness. The large in-plane size of the alloy film facilitated our straining experiment. The in-house developed in situ setup of Raman spectrophotometer combined with nanoindenter and scanning probe microscope have been used to correlate structure with mechanical deformation. Atomic-level insight into elastic deformation, plasticity, and fracture in $MoWSe_2$ is obtained from complementary molecular dynamics (MD) simulations performed using quantum mechanically informed empirical force fields. The theoretically predicted crack-induced phase transformation is verified with in situ electron beam exposure from high-angle annular dark-field (HAADF) STEM imaging.
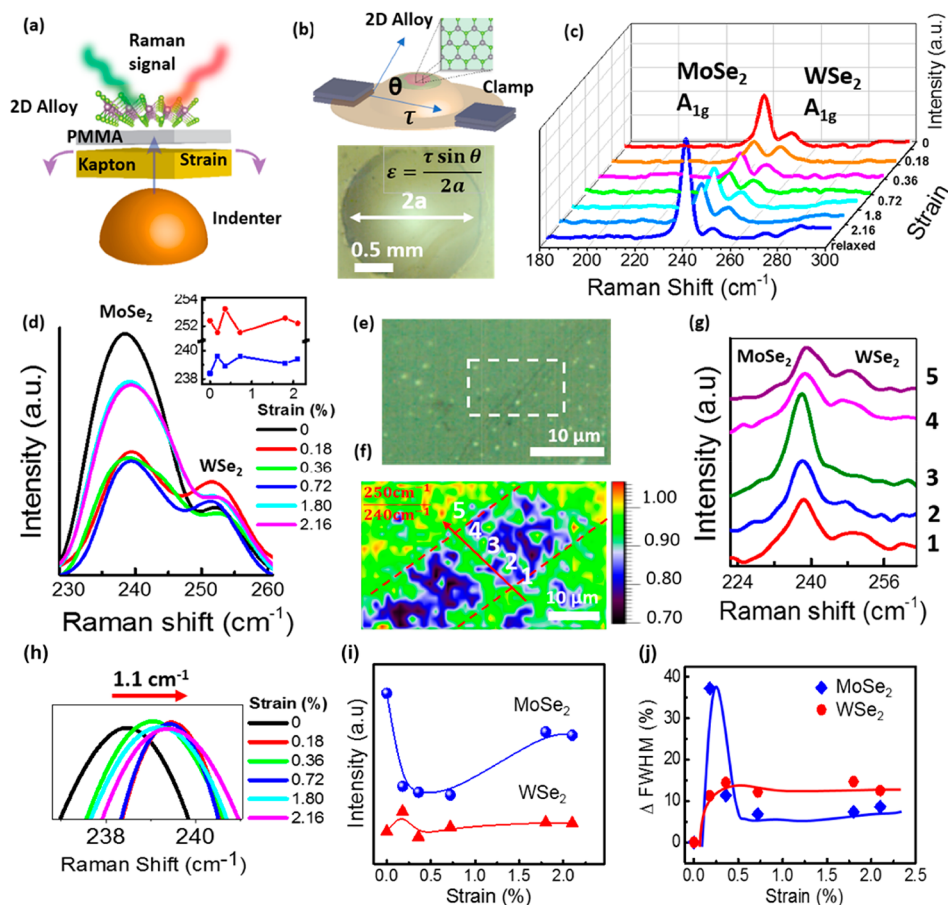
RESULTS/DISCUSSION

2D $MoWSe_2$ alloy films were grown on (0001) sapphire substrates using CVD as shown schematically in Figure 1a. The optical micrographs (Figure 1b,c) show the contrast between the film and the transparent sapphire substrate (the whole substrate is ~1 cm) illustrating the large area and continuous nature of the film. An AFM image near the boundary of the film is shown in Figure 1d. A line-scan on the sample edge reveals the step height as approximately ~0.7 nm, which is in agreement with values for monolayer TMDs.[13,14] Figure 1e,g shows the spot Raman and photoluminescence (PL) spectra; the two sharp peaks occurring at 239 and 249 cm^{-1} are attributed to the A_{1g} vibration modes of the out-of-plane Se–Mo–Se and Se–W–Se bonds, respectively. The hump at roughly 285 cm^{-1} is due to the in-plane E^1_{2g} mode of the Mo–Se–Mo bonds.[13,15] Bulk synthesis of such alloys is expected to result only in a single A_{1g} mode at intermediate frequency given the isomorphous nature of $MoSe_2$ and WSe_2.[16] The presence of two predominantly distinct modes in $MoWSe_2$ is more reminiscent of WSe_2 precipitates in $MoSe_2$, that is, a precipitate

Figure 1. Growth and characterization of 2D $MoWSe_2$ alloy. (a) Schematic of CVD growth. (b, c) Optical image of 2D $Mo_xW_{1−x}Se_2$ alloy grown on sapphire. (d) AFM image showing thickness of ~0.7 nm. (e) Raman spectrum, (f) Raman maps, and (g) PL spectrum of the alloy showing characteristic $MoSe_2$ and WSe_2 A_{1g} Raman modes and band gap of ~1.55 eV. The spectra were collected from the indicated spot in (c). (h) HAADF STEM Z-contrast image of the 2D alloy. (i) EEL spectra are taken from the red and yellow square regions in (h), showing that the regions are Mo-rich and W-rich, respectively. (j) Integrated intensity from the W O-edge prepeak, showing the formation of W-precipitates in the $MoSe_2$ lattice.
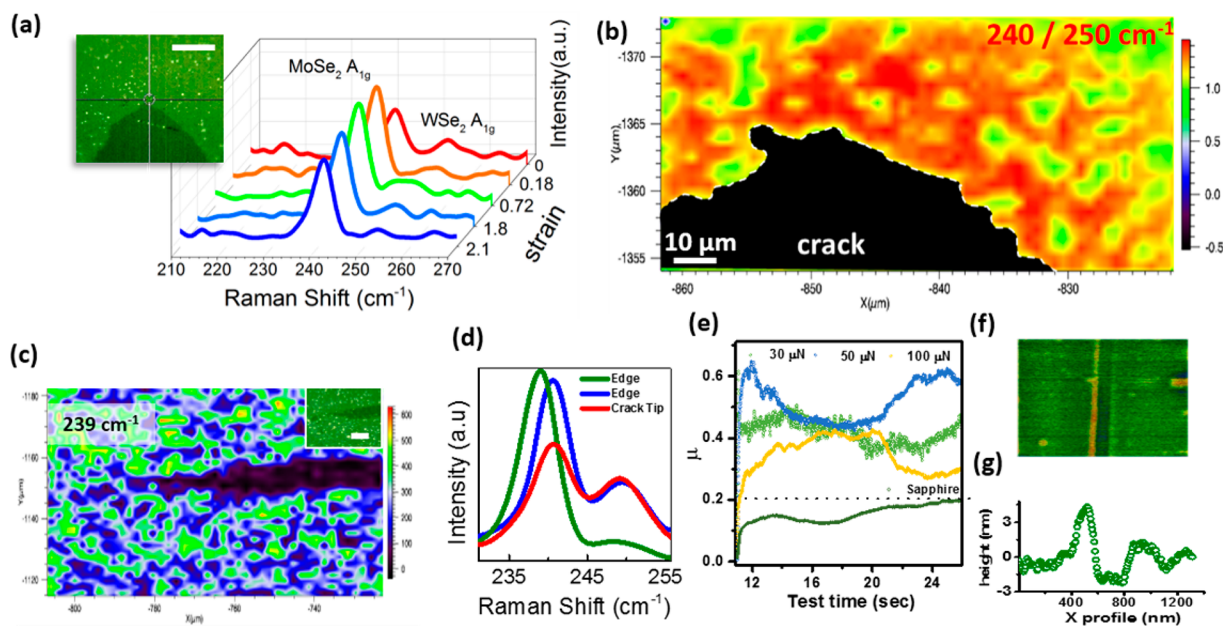
alloy.[17,18] The PL spectrum in Figure 1g shows the emission at 1.55 eV which is expected for the selenide TMDs and indicates an average value outcome from alloying. For better illustration, a section of the monolayer film was mapped at the two Raman peaks of 239 and 249 cm^{-1}, respectively, which show the distinct boundary between the films and the sapphire substrate (Figure 1f). To confirm and quantify the presence of the three constituent elements, X-ray photoelectron spectroscopy of the sample was performed; the results shown in SI Figure 1a–c illustrate the molybdenum $3d_{5/2}$ (229.1 eV) and $3d_{3/2}$ (232.2 eV), selenium $3d_{5/2}$ (54.9 eV) and $3d_{3/2}$ (55.7 eV), and tungsten $4f_{7/2}$ (32.7 eV) and $4f_{5/2}$ (35.1 eV) photoelectron peaks at the expected binding energies, respectively. These data indicate that molybdenum and tungsten are present in their Mo^{4+} and W^{4+} oxidation states. This is supported from the $Se^{2−}$ chemical shift to make up the MX_2-type stoichiometry. The average atomic concentration ratio between Mo and W elements as calculated from the Mo^{4+} and W^{4+} peaks was ~2:1 which is in close agreement with the intensities of their characteristic Raman modes in Figure 1e. Figure 1h shows a HAADF STEM image of a monolayer region of the alloy film.

Figure 2. Strain engineering and Raman spectroscopy probing of 2D MoWSe$_2$ alloy: (a, b) Schematics of the loading experiment. (c) Raman spectra as a function of increasing strain. The zoomed behavior of the two A$_{1g}$ modes is shown in (d); inset of (d) shows the variation of A$_{1g}$ mode frequencies as a function of strain. (e) Optical image of strain lines in alloy + PMMA and (f) Raman ratio map of indicated region showing dearth of WSe$_2$ signal in the strain-affected region. (g) Raman spectra of five points labeled across the strain line in (f) showing how WSe$_2$ signal flattens in between the strain lines. (h) Variation in the frequencies of the two A$_{1g}$ modes as a function of strain. (i) Variation in intensity of the two A$_{1g}$ modes as a function of strain; the MoSe$_2$ mode undergoes more drastic change than the WSe$_2$ one. This is also reflected in the variation in the fwhm's of the two modes as shown in adjoining subfigure (j); the lines represent guides to the eye for understanding the variation.

Here, sharp changes in contrast are visible within the alloy, and to determine the nature of those contrast changes and observe the W distribution in the alloy, electron energy loss spectroscopy (EELS) is performed on the region. EEL spectra are taken from two separate areas in the alloy exhibiting different contrasts, and the spectra are plotted in Figure 1i. All three elements are present in both regions: the Mo N-edge at 35 eV, the W O-edge at 36 eV, and the Se M-edge at 57 meV. The W and Mo edges in this region overlap significantly, but the W O-edge has a characteristic prepeak at the edge onset that distinguishes it from the mostly overlapping Mo N-edge. Both spectra exhibit a large peak with an onset at around 35−36 eV, but the presence of the W O-edge prepeak in the yellow spectrum indicates this region is W-rich, while the absence of the prepeak in the red spectrum indicates the region is Mo-rich. A spectrum image (SI) is obtained from this region, where EEL spectra are taken from each position in the region of interest. From the SI, the EELS intensities of individual spectral features (such as the W O-edge prepeak) can be integrated and plotted to form 2D maps of the feature in the region of interest. Figure 1j shows the SI map of the W O-edge prepeak and illustrates the distribution of W in the sample. It can be seen the precipitates of W-rich region are found throughout the sample.

Figure 2a,b illustrates the strain engineering experimental set up (details are described in Methods/Experimental Section). The waterfall plot in Figure 2c depicts the Raman spectra of the sample (all taken from the same ~1 μm spot) as a function of applied load/strain. The Raman spectra of the selenide monolayer between 230 and 260 cm^{-1} are made up of strong A$_{1g}$ resonances; these are the symmetric vibrations of the Se−Mo−Se and Se−W−Se bonds in the out-of-plane (z) direction, that is, in a direction perpendicular to the 2D sheet, as opposed to the E$^1_{2g}$ modes which indicate the in-plane motion. Therefore, as bending strain is applied to a 2D sheet, the out-of-plane vibrational modes are expected to show variations in frequencies, intensities, widths, *etc*. Since the two modes occur at quite close wavenumbers, the close-up of the spectra is shown in Figure 2d to better understand these variations. Increasing strain changes the A$_{1g}$ mode intensity and peak position for both MoSe$_2$ and WSe$_2$. As the strain is increased from 0 to 0.18%, the MoSe$_2$ A$_{1g}$ peak blue shifts by ~1.1 cm^{-1} and WSe$_2$ A$_{1g}$ modes red shifts by ~1 cm^{-1}. In addition, a drop-in intensity is observed for MoSe$_2$, A$_{1g}$ peak. Further increase in strain (0.18% to 0.36%) broadens the MoSe$_2$ mode, and a shoulder is seen at 245 cm^{-1}. WSe$_2$ mode blue shifts (from 251 to 253 cm^{-1}). At 0.72% strain, MoSe$_2$ A$_{1g}$ mode blue shifts by

Figure 3. Monitoring crack formation and propagation in 2D MoWSe$_2$ alloy. (a) Raman spectra at the notch of a blunt crack as a function of strain (inset scale bar = 10 μm). (b) Raman ratio map of blunt crack showing mostly MoSe$_2$ signals at the notch. (c) Raman map of MoSe$_2$ A$_{1g}$ mode of a sharp propagating crack shown in the inset (scale bar = 20 μm). The Raman spectra at the two crack edges and the tip are shown in (d). (e) Scratch test of the 2D alloy showing variations in friction coefficient traces as a function of applied load. (f) Scanning probe image of static scratch in 2D alloy on sapphire and (g) accompanying height profile.

1.3 cm^{-1}, whereas WSe$_2$ one red shifts (from 253.1 cm^{-1} to 251.5 cm^{-1}). At higher strains (1.8% and 2.1%), an increase in intensity is observed for A$_{1g}$ in MoSe$_2$, while WSe$_2$ mode intensity does not vary significantly. Variations of MoSe$_2$ and WSe$_2$ A$_{1g}$ peak positions as a function of strain are shown in the inset of Figure 2d. The complicated variation is due to the increasing levels of strain being steadily accommodated inside the 2D lattice. As seen in Figure 2d, the spectral region between 240 cm^{-1} and 250 cm^{-1} for strain equal to 0.18%, 0.36%, and 0.72% is asymmetric, that is, A$_{1g}$ peak in MoSe$_2$ develops a shoulder. Hence, we performed curve fitting in this region (SI Figure 2a–c). Apart from the two A$_{1g}$ peaks of MoSe$_2$ and WSe$_2$, at 0.18% strain, a new peak at 244 cm^{-1} emerges (SI Figure 2a), and it intensifies at a strain of 0.36% (b) while undergoing a ∼ 2 cm^{-1} red-shift and gradually reduces when the strain is 0.72% (c), disappearing thereafter at higher strain values (1.8% and 2.16%). This peak is attributed to the vibrations of Se atoms bonded to Mo and W atoms, that is, alloying as reported in ref 14. However, in our CVD-grown 2D alloy, the individual A$_{1g}$ vibrations indicate MoSe$_2$- and WSe$_2$-rich regions. Figure 2i shows how the intensities of the two modes vary as the strain increases. As the strain increases, there is a significant change in intensity of the MoSe$_2$ mode followed by saturation (at intermediate strain), implying that the strain is initially distributed more in the Se−Mo−Se bonds before the Se−W−Se bonds are affected to similar degree. We are considering the intensity variations between successive strain values, as we know that the absolute intensity values of the two modes are different. Next, we examine the variations in the fwhm's of the two modes. The fwhm of a Raman mode contains information about plastic deformation as well as instantaneous changes to crystallinity as probed from the spot size. Figure 2j shows that the fwhm of the MoSe$_2$ A$_{1g}$ mode undergoes a sudden increase relative to the WSe$_2$ one; a clear indication that the applied load is dispersed through the Mo

atoms in the monolayer as opposed to the W ones. Thus, the strain affects both vibrational modes differently in a monolayer alloy. As the fwhm of Raman modes relates to the degree of crystallinity of the material, amorphous materials have broader peaks, whereas crystalline ones exhibit sharp resonances. It is possible that the monolayer crystallinity is instantaneously affected as the material gathers and disperses the strain in two dimensions most likely in conjunction with the new intermediate peak developing and indicating dynamic diffusion. When the alloy monolayer is strained, the Se−Mo−Se bonds bear most of the load, and, therefore, the corresponding A$_{1g}$ mode is affected more severely than the one for the Se−W−Se bonds.
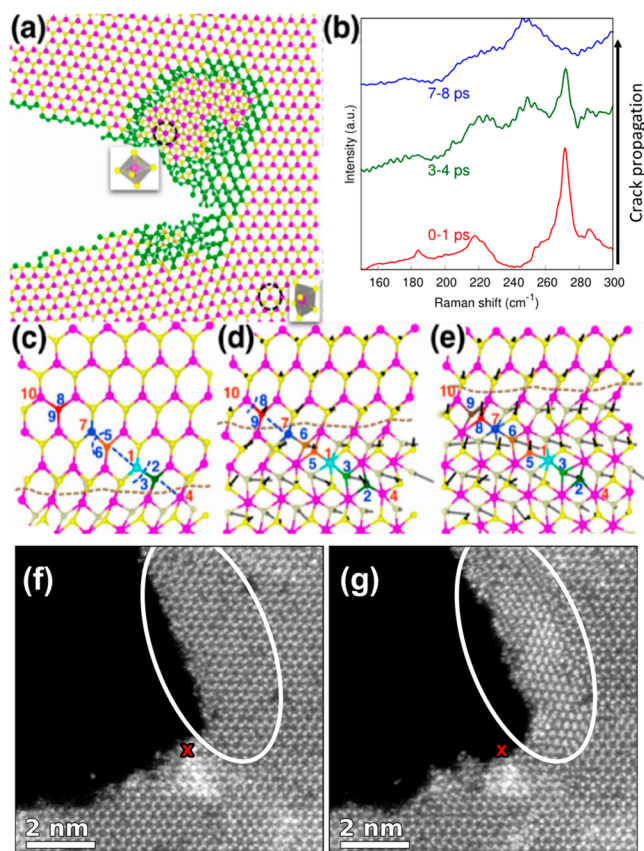
MD simulations were performed to understand these observed strain-induced changes in structure and bonding in the MoWSe$_2$ alloy. The MD simulations were based on a Stillinger−Weber force field parametrized with density functional theory (DFT) calculations of the structural and mechanical properties of MoSe$_2$ and WSe$_2$ crystals and validated with experimental data. The MD simulations on pure MoSe$_2$ monolayers indicate that the Mo−Se bond length is 2.53 Å. In the strained MoSe$_2$ monolayer, the bond length increases to as much as 2.7 Å near the tip of a subcritical crack. In pure WSe$_2$, the bond length in the unstrained crystal is 2.54 Å, and near the tip of a subcritical crack, the bond length can be as large as 2.68 Å. The optical image in Figure 2e shows a set of striation lines (plastically deformed region) propagating in a near-parallel fashion through the monolayer film as indicated inside the white bounding rectangle; these lines were observed at 2.16% strain. Here, the monolayer film inside the white rectangle was chosen for mapping the Raman intensity of the two A$_{1g}$ modes. A map of the ratio of the two individual intensities (WSe$_2$/MoSe$_2$ A$_{1g}$ ratio) is shown in Figure 2f. Between the strain lines (marked by red dotted lines) the 2D alloy most likely changes structure to accommodate volume

change. In addition, it is not just that the sharp intensity drop is confined to the cracks but spreads a couple of microns away from them in the planar directions. At this level, the optical setup of the Raman microscope becomes the limiting factor due to the Rayleigh limit and the step size of the hyperspectral image. Across the strain line (marked by numbers 1−5 along the red arrow in Figure 2f), the Raman spectra are extracted and plotted in Figure 2g. The variation of $MoSe_2$ and WSe_2 A_{1g} modes is plotted in Figure 2g. In plastically deformed regions, the Se−W−Se vibrations are completely damped in these regions (blue color) implying that the strain is preferentially affecting the tungsten selenide regions of the monolayer alloy. It is also important to consider the $MoSe_2$ and WSe_2 precipitate size distribution. As seen in Figure 1h, the $MoSe_2$ precipitates are larger in size. In between $MoSe_2$, WSe_2 clusters are seen (which are smaller in size). The interfaces between $MoSe_2$ and WSe_2 act as local heterojunctions where Se atoms bind with both Mo and W atoms. When strain is applied to the 2D alloy, the fwhm of molybdenum bond vibrations undergo a 38% difference between the unstrained and strained points, as opposed to only 13% for the tungsten bonds (Figure 2j). Mismatched $MoSe_2$ and WSe_2 local deformation can induce a tensile strain on WSe_2 crystals and affect the Se−W−Se vibrations (blue shift). At higher strain values, the strains are uniformly distributed in WSe_2 crystals and as seen in Figure 2j,f; the wavenumber and fwhm do not vary drastically. Figure 2f gives an indication that in such a 2D alloy, the defects propagate easily through WSe_2 regions.

To examine crack propagation in the 2D $MoWSe_2$ alloy, we introduced two types of cuts (blunt and sharp notch) and monitored crack growth at different applied strains. A sharp diamond Berkovich indenter was used to create the cut or notch in the 2D alloy. Raman spectra recorded from the crack-tip region at different strains are shown in Figure 3a. The top right inset shows the optical image of the blunt crack. $MoSe_2$/WSe_2 A_{1g} Raman intensity ratio map recorded from crack-tip region at 2.16% strain is shown in Figure 3b. A_{1g} modes of $MoSe_2$ and WSe_2 are hardened by 2 cm^{-1} as soon as the load sets in ($MoSe_2$ A_{1g} from 239 to 241 cm^{-1}, WSe_2 A_{1g} from 249 to 251 cm^{-1}). The spectra and map conclude that the Se−W−Se A_{1g} mode adjacent to the crack is significantly damped. Therefore, even after the crack has propagated, the resulting strain has affected Se−W−Se bonds in the surrounding region (up to a range of nearly 10 microns). The dark green spots in the $MoSe_2$ A_{1g} map (241 cm^{-1}, SI Figure 3a) are due to small multilayer islands (yellow dots in the optical image in 'a') on top of the large-area monolayer film and are a natural outcome of the CVD growth process. The presence of additional layers shifts the bond vibration frequencies, and as a result, those regions appear devoid of intensity for the map corresponding to the values for the monolayer. There could also be a contribution from strain affecting the thicker multilayers by different amounts compared to the larger monolayer film. The inset of Figure 3c shows an optical image of a freshly opened sharp crack at 2.16% strain. Raman intensity mapping of the $MoSe_2$ A_{1g} mode from this region is shown in Figure 3c. Raman spot spectra recorded from three different regions of the crack (indicated as 1−3) are shown in Figure 3d. We see that the spectra at the extreme ends bear A_{1g} modes from both $MoSe_2$ and WSe_2, whereas the signal from the WSe_2 mode falls significantly on the edges of the crack. This is another evidence that the edges of the crack (which are the more interesting regions compared to the bulk of the crack) lie in $MoSe_2$-rich
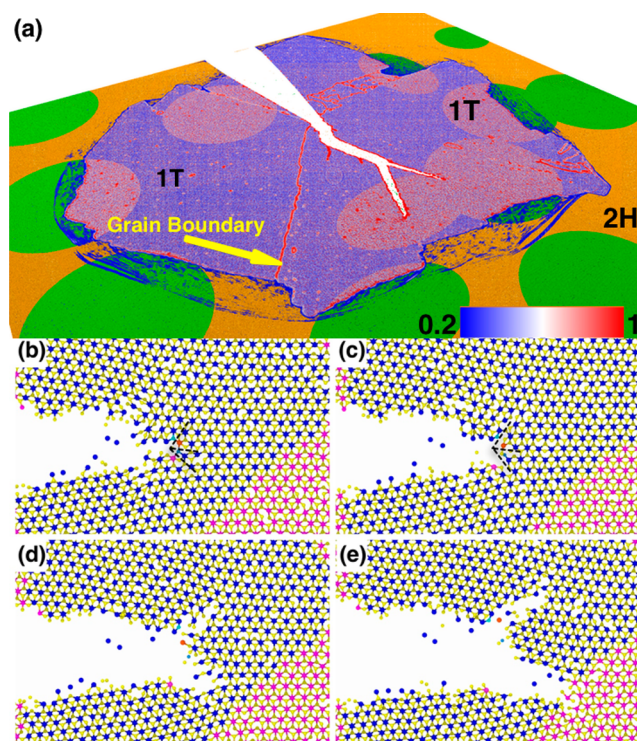
regions. It is equally interesting to study the deformation behavior of the $MoWSe_2$ alloy in steady state. A sample as grown on sapphire was separately tested using a nanoscratch device (Tribo indenter, Bruker Nano Surfaces, USA). Using the sharp diamond Berkovich indenter, 10 μm long scratches were made on the 2D alloy at different applied normal loads. The friction coefficients recorded at different normal loads are shown in Figure 3e, and the corresponding SPM image of the scratched sample (100 μN) is shown in Figure 3f. At loads <50 μN, the 2D alloy was intact and recorded high friction, reflecting the $MoWSe_2$ alloy's resistance to lateral deformation. At 100 μN, the scratch depth was ∼1.5 nm (Figure 3g). The $MoWSe_2$ alloy had ∼0.7 nm thickness prior to scratching. The friction trace was influenced by substrate at a 100 μN load. Raman map recorded from a 100 μN scratch is shown in SI Figure 3c,d.

MD simulations were also performed to examine vibrational modes and atomistic mechanisms of defect formation, phase change, and crack propagation in the strained $MoWSe_2$ alloy. The system consists of an $MoSe_2$ monolayer containing regions of WSe_2 distributed randomly in the $MoSe_2$ matrix. The fraction of WSe_2 in $MoSe_2$ is the same as in the experiment. MD simulations were performed on a system of size 0.5 μm × 0.5 μm. The $MoSe_2$ matrix has a precrack of length 0.166 μm. The boundaries of the system are clamped, and a strain is applied perpendicular to the precrack. The strain rate is 2.25×10^7 s^{-1}, and the system is relaxed for 100 ps after each incremental change (0.225%) in strain. Here, we present MD results for crack propagation and time-resolved Raman spectra. Figure 4a shows snapshots of crack propagation and process zone at a strain of 2.15%, which corresponds to the onset of crack propagation. The crack meanders slightly as it propagates through the $MoSe_2$ matrix by breaking Mo−Se bonds. The precrack branches into daughter cracks as it crosses the $MoSe_2$/WSe_2 interface and enters the WSe_2 patches (Figure 5a,b). The most dramatic change occurs in the process zone around the crack tip, where large stress concentration and the resulting biaxial tensile strain trigger an irreversible local structural phase transformation (Figure 4a) from the ground-state 2H crystal structure to the 1T crystal structure. This is consistent with previous theoretical predictions and experimental observations in other elastically strained TMDCs.[19,20] Figure 4b shows the simulated Raman spectra from the 2H and 1T regions of the $MoWSe_2$ monolayer. Raman spectra are obtained from a calculation of the Fourier transform of the group breathing autocorrelation functions.[21] These autocorrelation functions are calculated from the atomic trajectories in the MD simulation of the 0.5 μm × 0.5 μm monolayer by projecting the relative velocity between each Mo/W cation and its neighboring Se anion along the direction of the cation−anion bond. This dynamical property is associated with bond stretching and can be used to accurately determine the frequencies of the Raman absorption peaks, however spectral intensities obtained from this method are unreliable, since information about Raman scattering cross sections is not considered. Time-resolved Raman spectra obtained during crack propagation through the $MoSe_2$/WSe_2 alloy monolayer show that spectra from the initial stages of crack propagation are characterized by peaks at 220 and 270 cm^{-1}. Spectra obtained after crack propagation through the sample reflect the stress redistribution and phase transformation through the emergence of a new intermediate peak at 250 cm^{-1}. This trend is also observed in the experiment. The Raman spectra at the crack tip and edges of

Figure 4. Stress-induced 2H-1T phase transformation near the tip of the propagating crack. (a) Snapshot of the 2H-1T phase transformation as the crack propagates through the MoSe$_2$/WSe$_2$ alloy. The highlighted region indicates the two different crystal structures in the process zone. Green atoms are at the interface of the 2H phase and the disordered 1T phase. (b) Simulated Raman spectra of the MoSe$_2$/WSe$_2$ alloy during crack propagation. Spectra obtained during the initial stages of crack propagation (0−1 ps) are characteristic of the 2H crystal structure of the MoSe$_2$/WSe$_2$ alloy, while spectra from later times are obtained from simulation cells with greater 1T content. (c−e) Snapshots from the MD simulation of atomic configurations in the process zone. These snapshots show atomic displacements corresponding to the motion of the 2H-1T phase transformation front (dashed brown line). Here Mo, Se, and W are shown in pink, yellow, and blue colors, respectively. The transformation of Mo atoms (1, 4, 7) to the 1T structure is due to the displacement of Se atoms (2, 3, 5, 6, 8, and 9) highlighted in (c−e). Dotted blue curve indicates bond breaking, and dotted blue lines show bond formation. For example, in (c) the formation of 1(Mo)-5(Se) bond and breaking of 1(Mo)-2(Se) and 7(Mo)-5(Se) bonds transforms 1(Mo, cyan) from 2H to 1T structure. The resultant 1T structure is shown in (d). During this transformation, the Se pairs 2−3 and 5−6 move in opposite directions as shown in (d). (f) HAADF-STEM image of MoWSe$_2$ alloy near a crack. Electron beam is positioned at red x and allowed to damage the sample to propagate a crack. (g) STEM-HAADF image after crack propagation. The damage from the electron beam causes the crack to propagate, and the highlighted region undergoes a phase transformation.

the strained alloy as shown in SI Figure 3b show a convoluted peak between 250 and 260 cm^{-1}. The curve fitting in SI Figure 3e−g reveals an intermediate peak at ∼250 cm^{-1} and agrees with the results of the MD simulations. The phase transformation accompanying the stress surrounding the crack propagation in the 2D alloy is imaged *via* atomic resolution

Figure 5. Local deformation around cracks and crack propagation mechanism in a strained MoSe$_2$/WSe$_2$ monolayer in the [1,1] configuration. (a) Local strains in the process zone, with red dots representing point and extended defects. (b−e) Crack propagation and crack branching mechanism in MoSe$_2$/WSe$_2$ monolayer. (b) At the crack tip, multiple W (orange)−Se (cyan), W (orange)−Se (light blue) and W (pink)−Se (light blue) bond-breaking leads to form defects at the crack tip along different directions, which eventually leads to crack branching in the material (c−e).

HAADF-STEM. Figure 4f shows a HAADF image of the MoWSe$_2$ alloy near a crack in the lattice. In order to propagate the crack, the electron beam is positioned on the alloy film at the edge of the crack (marked by the green X). The high-energy electrons damage the alloy in a highly localized area and, after prolonged exposure, cause the crack to propagate, inducing stress in the film. After a 20 s exposure, a second HAADF image is acquired of the same region shown in Figure 4g. By comparing the position of the red X, it can be seen that the crack has propagated further toward the bottom-right corner of the image, and more importantly a phase transformation has occurred in the region next to the crack (highlighted by the white line).

Polymorphs like 2H and 1T are common in the TMDC family of materials and differ in the coordination of chalcogen atoms around the central transition-metal atom. The 2H crystal structure results from an A-B-A-type stacking in the chalcogen-transition metal-chalcogen trilayer leading to a trigonal prismatic coordination around the central Mo ion (Figure 4a, bottom inset). The 1T crystal structure arises from an A-B-C-type stacking of chalcogen-transition metal-chalcogen trilayer resulting in a distorted octahedral coordination around the central Mo ion (Figure 4a, top inset). The 1T crystal structure, with a larger lattice constant, is metastable, but becomes energetically favorable under high biaxial tensile strains. This stress relieving 2H-1T phase transformation proceeds primarily *via* the in-plane gliding of one of the chalcogen layers in the armchair direction (Figure 4c,e), identical to atomic mecha-

nisms observed in 2H-1T phase transformations in other TMDC materials.[22] Experimental evidence of stress-induced phase transitions in other ternary TMDC alloys has been observed and is included in the Supporting Information. We also calculate strains from MD trajectories using a local deformation analysis technique[23] and analyze the ring structures of Mo, W, and Se atoms to identify atomic and extended defects in the process zone.[24] These defects, denoted by green dots in Figure 5a, are distributed throughout the process zone, more so at the interface between the 2H and 1T phases (see Figure 4b,e). As the following discussion shows, these point defects play an important role in controlling the crack branching mechanism and therefore significantly affect the toughness of the monolayer material. In addition to these atomic defects, secondary cracks (red lines in Figure 5a) nucleate from the sides of the precrack and propagate through the 1T phase of the process zone. The crack-branching mechanism offers insight into the increased toughness of the MoWSe$_2$ alloy. Crack propagation occurs through the cleavage of Mo–Se and W–Se bonds at the crack tip due to the intense stress concentration (with σ_{yy} approaching 16 GPa at the MoSe$_2$/WSe$_2$ interface, as seen in SI Figure 4). Figure 5b–e shows successive snapshots of atomic configurations near the crack tip in the WSe$_2$ patch from the MD simulations, which demonstrate that crack growth leads to the nucleation of point defects in the process zone on either side of the propagating crack tip. These defects subsequently coalesce to create a preferred path for crack propagation, leading to the formation of multiple crack branches in the 2D monolayer. Additional observations from the MD simulations supporting the increased toughness of the alloyed monolayer are the following:

(1) The area of the process zone accompanying the growing crack is smaller in the MoWSe$_2$ alloyed system (SI Figure 5). The average velocity of the process zone front (defined as the boundary between the 2H and 1T phases) was calculated to be 2.7 ± 0.5 km s^{-1} in the pure MoSe$_2$ monolayer and 2.2 ± 0.6 km s^{-1} in the MoWSe$_2$ alloy. Consistent with the anisotropic distribution of local stresses in the process zone, this process zone growth is much faster along the direction of crack growth. The measured process zone velocity in front of the crack is 3.5 ± 0.3 km s^{-1} in the pure MoSe$_2$ monolayer and 2.6 ± 0.3 km s^{-1} in the alloy, which is consistent with the increased toughness of the MoWSe$_2$ alloy.

(2) More significantly, the rate of crack growth, as measured from MD simulations on systems of size 0.15 μm × 0.15 μm, is smaller in the case of the MoWSe$_2$ alloy (crack velocity = 1.95 km s^{-1}) than in the case of the pure, unalloyed MoSe$_2$ monolayer (crack velocity = 2.2 km s^{-1}).

(3) As shown in Figure 5a, in addition to local defects, we also observe grain boundaries in the 1T structure of the strained MoSe$_2$ matrix.

(4) These observations have been included in Videos S1 (stress) and S2 (fracture) and Supporting Information.

CONCLUSIONS

Large-area, continuous monolayer 2D molybdenum tungsten diselenide alloy was synthesized on a single-crystal (0001) sapphire substrate using chemical vapor deposition. The film was characterized using optical microscopy, atomic force microscopy, and Raman and photoluminescence spectroscopy

to ascertain its monolayer nature. X-ray photoelectron spectroscopy revealed the average alloy composition as Mo:W = 2:1. High-resolution imaging of the monolayer film was carried out *via* scanning transmission electron microscopy to understand nanoscopic composition and atomic distribution. The alloy film on flexible substrate was subjected to straining experiments to understand its response *via* Raman spectroscopy. Strain lines appeared upon further increase in strain, indicating plasticity in the sample, and we observed a dearth of tungsten atoms relative to molybdenum near strain lines. This was confirmed with local Raman intensity and ratio maps from regions close to stressed regions of the film as well as cracks/fractures. MD simulations and atomic resolution HAADF-STEM imaging reveal that crack growth in the alloy is accompanied by a structural phase transformation from the 2H to the 1T phase in the process zone around the crack. Raman spectra calculated from MD simulations of the crack propagation confirm the emergence of new intermediate peaks in the strained monolayer alloy, mirroring experimental results.

METHODS/EXPERIMENTAL SECTION

In a 2 in. quartz tube, a mixture of MoO$_3$ and WO$_3$ powders was loaded into a porcelain crucible covered with the sapphire substrates, as shown in Figure 1a. Another porcelain boat filled with selenium powder was placed upstream. The tube was filled with a mixture of Ar/H$_2$ gas at 100 sccm, heated to 875 °C for 15 min, and cooled down to ambient temperature. The monolayer films were obtained on the bottom surface of the sapphire (SI Figure 1). Raman and PL spectra were recorded on a Renishaw inVia confocal spectro-microscope with a 50× objective and 532 nm laser. XPS spectra were recorded on a PHI Quantera II with 1.486 keV incident energy and 26 eV pass energy. AFM was performed on a Bruker Multimode 8 in tapping mode. STEM-HAADF imaging was achieved on a Nion Ultra-STEM 100 at 60 kV with aberration correction.[25]

For the straining experiments, first the monolayer thin-films on sapphire were coated with poly(methyl methacrylate) (PMMA) and heated up to 55 °C on a hot plate for 10 min, followed by etching in hot KOH solution (2M) and delamination in cold DI water. The floating 'PMMA + monolayer thin-film' was scooped on to an SiO$_2$/Si substrate and immediately picked up with the sticky side of a Kapton tape to ensure smooth, bubble-free adhesion. *In situ* straining experiments were performed using a custom-built indenter (Bruker Nano Surfaces). A three-point bending method was used to apply strain. The Kapton tape with 2D alloy was firmly clamped at the two ends. A 2 mm sapphire ball mounted on to a precision linear actuator was used to push the 2D MoWSe$_2$ alloy. The strain on the sample was varied (0–2.1%) by changing ball displacement.

The monolayer film was transferred from the sapphire substrate on to a soft PMMA film (see experimental details above) which was then supported on top of a transparent Kapton tape. A three-point bending geometry was adapted for strain experiments. Two ends of the Kapton tape were clamped firmly, and the load was applied to the sample from underneath using indentation device. Figure 2b shows the contact image at peak strain. The indenter displacement was converted to strain values *via* the following equation:

$$\varepsilon = \frac{\tau \sin \theta}{2a}$$

MD simulations were performed on a MoSe$_2$ monolayer of dimensions 0.5 μm × 0.5 μm containing randomly distributed regions of WSe$_2$. The boundaries of the MoSe$_2$ matrix are clamped on all sides (atoms within 20 Å from the edges are kept fixed at each strain), and an atomically sharp precrack of length 166 nm is inserted in the matrix by removing Mo and Se atoms. The MD simulations are based on a Stillinger–Weber type of force field that was optimized with DFT calculations and experimental measurements of structural and

mechanical properties of MoSe$_2$ and WSe$_2$ (see Supporting Information). The force field was validated by comparing the calculated value of fracture toughness (K_{1c}) with experimental estimates for MoSe$_2$ and WSe$_2$ monolayers.

ASSOCIATED CONTENT

ⓈSupporting Information

The Supporting Information is available free of charge on the ACS Publications website at DOI: 10.1021/acsnano.8b00248.

> Experimental details and data: XPS spectra of as-grown sample, Curve-fitted Raman spectra of strained sample, further results about crack propagation and strain-induced *vs* electron-beam damage effects on sample (PDF)
> Video S1: Simulated stress distribution in the 2D alloy (AVI)
> Video S2: Simulated fracturing of 2D alloy (AVI)

AUTHOR INFORMATION

Corresponding Authors
*E-mail: rkalia@usc.edu.
*E-mail: cst.iisc@gmail.com.
*E-mail: ajayan@rice.edu.

ORCID ⓞ
Vidya Kochat: 0000-0002-6144-3732
Aravind Krishnamoorthy: 0000-0001-6778-2471
Praveena Manimunda: 0000-0002-1851-4777
Priya Vashishta: 0000-0003-4683-429X
Aiichiro Nakano: 0000-0003-3228-3896
Chandra Sekhar Tiwary: 0000-0001-9760-9768

Author Contributions

$^{\#}$These authors contributed equally. A.A. synthesized and characterized the samples. A.A., V.K., P.M., S.A.S.F. and C.S.T. designed and carried out the straining experiments. J.A.H. and J.C.I. carried out STEM-HAADF imaging and EELS. P.R., A.K., A.N., R.K.K., and P.V. designed and carried out the MD simulations. P.V., C.S.T., and P.M.A. advised the work.

Notes

The authors declare no competing financial interest.

This manuscript has been authored by UT-Battelle, LLC under contract no. DE-AC05-00OR22725 with the U.S. Department of Energy. The United States Government retains and the publisher, by accepting the article for publication, acknowledges that the United States Government retains a nonexclusive, paid-up, irrevocable, worldwide license to publish or reproduce the published form of this manuscript, or allow others to do so, for United States Government purposes. The Department of Energy will provide public access to these results of federally sponsored research in accordance with the DOE Public Access Plan (http://energy.gov/downloads/doe-public-access-plan). The authors declare no competing financial interest.

REFERENCES

(1) Novoselov, K. S.; Jiang, D.; Schedin, F.; Booth, T. J.; Khotkevich, V. V.; Morozov, S. V.; Geim, A. K. Two-Dimensional Atomic Crystals. *Proc. Natl. Acad. Sci. U. S. A.* **2005**, *102*, 10451−10453.

(2) Feng, Y.; Zhang, K.; Wang, F.; Liu, Z.; Fang, M.; Cao, R.; Miao, Y.; Yang, Z.; Mi, W.; Han, Y.; Song, Z.; Wong, H. S. P. Synthesis of Large-Area Highly Crystalline Monolayer Molybdenum Disulfide with Tunable Grain Size in a H2 atm. *ACS Appl. Mater. Interfaces* **2015**, *7*, 22587−22593.

(3) Butler, S. Z.; Hollen, S. M.; Cao, L.; Cui, Y.; Gupta, J. A.; Gutierrez, H. R.; Heinz, T. F.; Hong, S. S.; Huang, J.; Ismach, A. F.; Halperin, E. J.; Kuno, M.; Plashnitsa, V. V.; Robinson, R. D.; Ruoff, R. S.; Salahuddin, S.; Shan, J.; Shi, L.; Spencer, M. G.; Terrones, M.; et al. Opportunities in Two-Dimensional Materials Beyond Graphene. *ACS Nano* **2013**, *7*, 2898−2926.

(4) Wang, Q. H.; Kalantar-Zadeh, K.; Kis, A.; Coleman, J. N.; Strano, M. S. Electronics and Optoelectronics of Two-Dimensional Transition Metal Dichalcogenides. *Nat. Nanotechnol.* **2012**, *7*, 699−712.

(5) Radisavljevic, B.; Radenovic, A.; Brivio, J.; Giacometti, V.; Kis, A. Single-Layer MoS2 Transistors. *Nat. Nanotechnol.* **2011**, *6*, 147−150.

(6) Kang, K.; Xie, S.; Huang, L.; Han, Y.; Huang, P. Y.; Mak, K. F.; Kim, C.-J.; Muller, D.; Park, J. High-Mobility Three-Atom-Thick Semiconducting Films with Wafer-Scale Homogeneity. *Nature* **2015**, *520*, 656−660.

(7) Bertolazzi, S.; Brivio, J.; Kis, A. Stretching and Breaking of Ultrathin MoS2. *ACS Nano* **2011**, *5*, 9703−9709.

(8) Lee, C.; Wei, X.; Kysar, J. W.; Hone, J. Measurement of the Elastic Properties and Intrinsic Strength of Monolayer Graphene. *Science* **2008**, *321*, 385−388.

(9) Akinwande, D.; Brennan, C. J.; Bunch, J. S.; Egberts, P.; Felts, J. R.; Gao, H.; Huang, R.; Kim, J. S.; Li, T.; Li, Y.; Liechti, K. M.; Lu, N.; Park, H. S.; Reed, E. J.; Wang, P.; Yakobson, B. I.; Zhang, T.; Zhang, Y.; Zhou, Y.; Zhu, Y. A Review on Mechanics and Mechanical Properties of 2D materials—Graphene and beyond. *Extrem. Mech. Lett.* **2017**, *13*, 42−77.

(10) Liu, K.; Yan, Q.; Chen, M.; Fan, W.; Sun, Y.; Suh, J.; Fu, D.; Lee, S.; Zhou, J.; Tongay, S.; Ji, J.; Neaton, J. B.; Wu, J. Elastic Properties of Chemical-Vapor-Deposited Monolayer MoS2, WS2, and Their Bilayer Heterostructures. *Nano Lett.* **2014**, *14*, 5097−5103.

(11) Island, J. O.; Kuc, A.; Diependaal, E. H.; Bratschitsch, R.; van der Zant, H. S. J.; Heine, T.; Castellanos-Gomez, A. Precise and Reversible Band Gap Tuning in Single-Layer MoSe2 by Uniaxial Strain. *Nanoscale* **2016**, *8*, 2589−2593.

(12) Lee, C.; Yan, H.; Brus, L. E.; Heinz, T. F.; Hone, J.; Ryu, S. Anomalous Lattice Vibrations of Single- and Few-Layer MoS2. *ACS Nano* **2010**, *4*, 2695−2700.

(13) Wang, X.; Gong, Y.; Shi, G.; Chow, W. L.; Keyshar, K.; Ye, G.; Vajtai, R.; Lou, J.; Liu, Z.; Ringe, E.; Tay, B. K.; Ajayan, P. M. Chemical Vapor Deposition Growth of Crystalline Monolayer MoSe2. *ACS Nano* **2014**, *8*, 5125−5131.

(14) Benameur, M. M.; Radisavljevic, R.; Héron, J. S.; Sahoo, S.; Berger, H.; Kis, A. Visibility of Dichalcogenide Nanolayers. *Nanotechnology* **2011**, *22*, 125706.

(15) Liu, B.; Fathi, M.; Chen, L.; Abbas, A.; Ma, Y.; Zhou, C. Chemical Vapor Deposition Growth of Monolayer WSe2 with Tunable Device Characteristics and Growth Mechanism Study. *ACS Nano* **2015**, *9*, 6119−6127.

(16) Zhang, M.; Wu, J.; Zhu, Y.; Dumcenco, D. O.; Hong, J.; Mao, N.; Deng, S.; Chen, Y.; Yang, Y.; Jin, C.; Chaki, S. H.; Huang, Y. S.; Zhang, J.; Xie, L. Two-Dimensional Molybdenum Tungsten Diselenide Alloys: Photoluminescence, Raman Scattering, and Electrical Transport. *ACS Nano* **2014**, *8*, 7130−7137.

(17) Gong, Y.; Lei, S.; Ye, G.; Li, B.; He, Y.; Keyshar, K.; Zhang, X.; Wang, Q.; Lou, J.; Liu, Z.; Vajtai, R.; Zhou, W.; Ajayan, P. M. Two-

Step Growth of Two-Dimensional WSe2/MoSe2 Heterostructures. *Nano Lett.* **2015**, *15*, 6135−6141.

(18) Huang, C.; Wu, S.; Sanchez, A. M.; Peters, J. J. P.; Beanland, R.; Ross, J. S.; Rivera, P.; Yao, W.; Cobden, D. H.; Xu, X. Lateral Heterojunctions within Monolayer MoSe2−WSe2 Semiconductors. *Nat. Mater.* **2014**, *13*, 1096−1101.

(19) Song, S.; Keum, D. H.; Cho, S.; Perello, D.; Kim, Y.; Lee, Y. H. Room Temperature Semiconductor-Metal Transition of MoTe2 Thin Films Engineered by Strain. *Nano Lett.* **2016**, *16*, 188−193.

(20) Duerloo, K. A. N.; Li, Y.; Reed, E. J. Structural Phase Transitions in Two-Dimensional Mo- and W-Dichalcogenide Monolayers. *Nat. Commun.* **2014**, *5*, 4214.

(21) Boulard, B.; Kieffer, J.; Phifer, C. C.; Angell, C. A. Vibrational Spectra in Fluoride Crystals and Glasses at Normal and High Pressures by Computer Simulation. *J. Non-Cryst. Solids* **1992**, *140*, 350−358.

(22) Lin, Y. C.; Dumcencon, D. O.; Huang, Y. S.; Suenaga, K. Atomic Mechanism of the Semiconducting-to-Metallic Phase Transition in Single-Layered MoS2. *Nat. Nanotechnol.* **2014**, *9*, 391−396.

(23) Falk, M. L. Molecular-Dynamics Study of Ductile and Brittle Fracture in Model Noncrystalline Solids. *Phys. Rev. B: Condens. Matter Mater. Phys.* **1999**, *60*, 7062−7070.

(24) Rino, J. P.; Ebbsjo, I.; Kalia, R. K.; Nakano, A.; Vashishta, P. Structure of Rings in Vitreous SiO2. *Phys. Rev. B: Condens. Matter Mater. Phys.* **1993**, *47*, 3053−3062.

(25) Krivanek, O. L.; Corbin, G. J.; Dellby, N.; Elston, B. F.; Keyse, R. J.; Murfitt, M. F.; Own, C. S.; Szilagyi, Z. S.; Woodruff, J. W. An Electron Microscope for the Aberration-Corrected Era. *Ultramicroscopy* **2008**, *108*, 179−195.